CrystEngComm

PAPER

Cite this: *CrystEngComm*, 2017, **19**, 3420

Influence of pH and citrate on the formation of oxalate layers on calcite revealed by *in situ* nanoscale imaging†

A. Burgos-Cara, *[a] C. V. Putnis,[bc] M. Ortega-Huertas [a] and E. Ruiz-Agudo [a]

Received 13th February 2017,
Accepted 5th June 2017

DOI: 10.1039/c7ce00305f

rsc.li/crystengcomm

The influence of pH and citrate concentration on the replacement of calcite by calcium oxalate has been investigated by *in situ* nanoscale observations in flow-through experiments performed using atomic force microscopy (AFM). Significant changes in the morphology of the precipitated whewellite ($CaC_2O_4{\cdot}H_2O$) crystals were observed, as well as in the degree of interface coupling of the dissolution–precipitation reactions, depending on the pH of the solution. Citrate also influences whewellite morphology; different citrate species seem to preferentially adsorb on different whewellite faces according to our experimental observations. The results of this study may help in the design of effective treatments for the protection of calcareous stone, based on the natural process of patina formation that occurs in monuments, as well as to better understand the process of unwanted oxalate precipitate formation and its control by small organic molecules such as citrate.

Introduction

Calcium oxalate minerals ($CaC_2O_4{\cdot}xH_2O$) are commonly found in fossils, plants and kidney stones.[1–4] They are also an unwanted by-product in some industrial processes such as paper manufacture, food and beverage production,[2,5–7] where calcium oxalate forms scale layers on the inner surfaces of tanks, pipes and heat exchangers, reducing the operation yields.[2,8] Calcium oxalate formation has been studied for many years, especially by urologists, as it is one of the main components of kidney stones that generate urinary tract diseases.[9] Three phases with different degrees of hydration are found in nature: $CaC_2O_4{\cdot}H_2O$ (Whewellite, COM), $CaC_2O_4{\cdot}2H_2O$ (Weddellite, COD) and $CaC_2O_4{\cdot}3H_2O$ (Caoxite, COT). Whewellite is the most thermodynamically stable polymorph and the primary constituent of more than 60% of human kidney stones,[1,9,10] together with phosphates.

Calcium oxalates and, in particular, whewellite, have been also observed in patinas on calcareous stone in historic buildings worldwide.[11–18] During the formation of oxalate surface layers on building stones, there is frequently a Ca-bearing mineral that is replaced by calcium-oxalate, whose crystallization is induced by the dissolution of the parent mineral that releases Ca^{2+} ions into the solution at the mineral–fluid interface, followed by the heterogeneous nucleation of calcium oxalate crystals, by a coupled dissolution–precipitation process.[19–21] Calcium oxalate has quite a low solubility (whewellite solubility is almost 20 times lower than that of calcite, 0.67 mg L^{-1} *vs.* 13 mg L^{-1}, respectively, at 20 °C). Because of the low solubility of calcium oxalate compounds, attempts have been made to use them as a protective treatment against chemical weathering of calcareous building materials in cultural heritage,[22–24] through the generation of less soluble oxalate layers by a mineral replacement process. Such treatments always rely on the partial dissolution of a thin surface layer of the stone surface that is replaced by the protective rim; *i.e.* the dissolution of the substrate is needed as a source of Ca ions for the precipitation of insoluble Ca.

Dissolution and precipitation reactions are the principal driving mechanisms for all mineral reequilibration reactions in the presence of a fluid phase.[19] When dissolution and precipitation are coupled at the interface between the mineral crystal surface and the aqueous solution, a pseudomorphic replacement is obtained.[25] An aqueous fluid may induce enough dissolution so that an interfacial boundary layer becomes supersaturated with respect to one or more new phases that can then precipitate spontaneously.[21] These conditions will be reached if dissolution is faster than diffusion of the dissolved species away from the mineral–fluid interface. If this interface-coupled dissolution–precipitation process results in less volume precipitated than dissolved, that is, it is a volume deficit reaction, porosity will form in the precipitated phase and this will allow the fluid to penetrate

[a] *Department of Mineralogy and Petrology, University of Granada, 18071 Granada, Spain. E-mail: aburgoscara@ugr.es*
[b] *Institut für Mineralogie, University of Münster, 48149 Münster, Germany*
[c] *Department of Chemistry, Curtin University, 6845 Perth, Australia*

† Electronic supplementary information (ESI) available. See DOI: 10.1039/c7ce00305f

further to the interface with the dissolving mineral. However, if more solid volume is precipitated than dissolved, the surface will become covered and effectively passivated by a thin rim of the product phase,[26] this preventing or slowing down further dissolution of the parent phase.

In order to generate functional protective rims for stone conservation purposes, full coverage of the substrate surface is required to avoid uncovered substrate areas where dissolution of the parent phase could still occur.[27] The formation of Ca-oxalate precipitates with small crystal sizes upon partial dissolution of the substrate, as well as other sparingly soluble Ca-bearing phases such as calcium phosphates[28] would allow an optimal reproduction of the initial substrate topography, thereby generating a more uniform and cohesive protective layer. The formation of calcium phosphate layers on calcite surfaces has been previously studied *in situ* and at high resolution using AFM.[29–31] The presence of additives in the replacement fluid may play an important role at modifying the precipitated crystal morphology and thus the form of the developed rim. Organic additives are well known to play a key role in influencing the formation of minerals in both biotic and abiotic systems, facilitating or inhibiting precipitation and subsequent growth and modifying crystal size and morphology.[32–36] Several studies have reported that additives such as small molecules (*i.e.* pyrophosphate, citrate or magnesium salts) and macromolecules (*i.e.* glycosaminoglycan, osteopontin, Tamm–Horsfall protein, nefrocalcina, urinary fragment 1 prothrombin or uropontin) have an inhibitory effect and/or are able to control calcium oxalate precipitation and growth.[37–43]

With this in mind, we have performed an experimental study of the replacement of calcite by calcium oxalate, given the common use of calcitic stones as building materials (*i.e.*, marble and limestone). In order to evaluate changes in the morphology of the precipitates and possible control on the distribution of such precipitates in the replacement rim by organic additives, citrate was selected because it is a naturally occurring organic molecule with a low molecular weight, being fully biodegradable and non-toxic.[44,45] Citrate plays an important role in biomineralization processes related to calcium oxalate, carbonate and phosphate compounds. Citrate has been proposed as a stabilizing agent of amorphous intermediate phases in biomineralization,[28,46–48] being able to reduce crystal sizes (*i.e.* calcium phosphate[28,49,50]), acting as a chelating agent. Citrate is also related to kidney stone formation, aggregation, and even dissolution.[40,51,52]

In this work we have explored the influence of citrate concentration and pH on calcium oxalate precipitation on calcite surfaces, with the aim of controlling the coupling of dissolution and precipitation at the reaction surface as well as modifying the precipitated crystal size and morphology. This has been done by atomic force microscopy (AFM), a commonly used technique to obtain *in situ* information about crystal growth and dissolution at the nanoscale (*e.g.* Ruiz-Agudo and Putnis, 2012).[53] Previous works report direct observations of whewellite growth in pure growth solutions and in the presence of organic compounds such as citrate.[54–56] A reduction in the whewellite growth rate and roughening of the step edges in the presence of citrate, suggesting the inhibitory role of citrate, was the main finding of these AFM studies. However, to our knowledge, there are no studies aimed at unraveling the effect of organic molecules on the replacement of calcite by calcium oxalate.

Materials and methods

Freshly cleaved calcite {10.4} surfaces (pure, clear crystals from Naica, Chihuahua, Mexico) were used as substrates for the *in situ* AFM experiments. Crystals of *ca.* 3 × 3 × 1 mm in size were cleaved directly prior to each experiment. Oxalic acid di-hydrate and tribasic sodium citrate with analytical reagent grade according to American Chemical Society (ACS) standards were used as reactants and obtained from Sigma-Aldrich. Test solutions were prepared freshly before every set of experiments and pH was adjusted (with HCl and/or NaOH of the same quality) by using a pH-meter with a glass electrode from Mettler-Toledo. All solutions were made using ultrapure water (type I+, resistivity 18.2 MΩ cm, Milli-Q®).

2.1 Flow-through experiments

Flow-through experiments were carried out using a Multimode IIIa Atomic Force Microscope (AFM, Digital Instruments, Bruker) equipped with a fluid cell type MTFML (Digital Instruments, Bruker). The AFM was used in contact mode at controlled room temperature (22.0 ± 0.5 °C). A semi-continuous solution flow was passed through the fluid cell by single syringe injections with an average flow rate of 500 μL s^{-1} before every image acquisition, resulting in an effective flow rate of *ca.* 85 mL per hour. AFM images were collected at a scanning frequency of 4.07 Hz using Si_3N_4 tips with a 45 nm coating of Ti/Au (Bruker, tip model SNL-10). Before every flow-through experiment, water was flowed through the fluid cell in order to clean the cleaved surface as well as to adjust the AFM parameters. Subsequent image processing was performed with the software Nanoscope from Bruker (Version 1.50) and geometrical measurements were made using the software AutoCAD 2014 with at least 30 measurements for each experimental condition. X-Ray diffraction (XRD) analysis of crystals collected after *in situ* AFM flow-through experiments was performed using a Philips X'Pert Pro X-ray diffractometer equipped with Cu Kα radiation (λ = 1.5405 Å) at 2θ range between 3° and 60° and at a scanning rate of 0.002° 2θ s^{-1} by placing the crystal in the diffractometer chamber with the (104) cleavage plane parallel to the sample holder.

2.2 Solution speciation calculations

Solution speciation calculations under the experimental conditions of the AFM study were carried out using the *PHREEQc* geochemical code.[57] The association constants and solubility products used in *PHREEQc* calculations are listed in Table 1. Calculations were performed considering that the dissolution and precipitation processes are confined to a fluid boundary

Table 1 Association constants and solubility product values used in PHREEQc simulations

Association constants[a] ($\log k$)	
$H^+ + C_2O_4^{2-} \rightleftharpoons HC_2O_4^-$	1.252
$H^+ + HC_2O_4^- \rightleftharpoons H_2C_2O_4^-$	4.266
$C_2O_4^{2-} + Ca^{2+} \rightleftharpoons CaC_2O_4$	3.44
$C_2O_4^{2-} + 2Ca^{2+} \rightleftharpoons Ca_2C_2O_4^{2+}$	5.29
$C_2O_4^{2-} + Ca^{2+} \rightleftharpoons Ca(C_2O_4)_2^{2-}$	4.68
$HC_2O_4^- + Ca^{2+} \rightleftharpoons CaHC_2O_4^+$	6.17
$H_2C_2O_4 + Ca^{2+} \rightleftharpoons CaH_2C_2O_4^{2+}$	11.1
$H^+ + Cit^{3-} \rightleftharpoons HCit^{2-}$	6.46
$2H^+ + Cit^{3-} \rightleftharpoons H_2Cit^-$	11.16
$3H^+ + Cit^{3-} \rightleftharpoons H_3Cit$	14.49
$Ca^{2+} + Cit^{3-} \rightleftharpoons CaCit^-$	4.75
$Ca^{2+} + H^+ + Cit^{3-} \rightleftharpoons CaHCit$	9.28
$Ca^{2+} + 2H^+ + Cit^{3-} \rightleftharpoons CaH_2Cit^+$	12.26
$Na^+ + Cit^{3-} \rightleftharpoons NaCit^{2-}$	1.35
$Na^+ + C_2O_4^{2-} \rightleftharpoons NaC_2O_4^-$	0.995
$2Na^+ + Cit^{3-} \leftrightarrow Na_2Cit^-$	1.5[b]
$Na^+ + H^+ + Cit^{3-} \rightleftharpoons NaHCit^-$	6.45[b]
Solubility products[c] ($\log k_{SP}$)	
$CaC_2O_4{\cdot}H_2O \rightleftharpoons C_2O_4^{2-} + Ca^{2+} + H_2O$	−8.69
$CaC_2O_4{\cdot}2H_2O \rightleftharpoons C_2O_4^{2-} + Ca^{2+} + 2H_2O$	−8.43
$CaC_2O_4{\cdot}3H_2O \rightleftharpoons C_2O_4^{2-} + Ca^{2+} + 3H_2O$	−8.28
$Ca_3Cit_2{\cdot}4H_2O \rightleftharpoons 3Ca^{+2} + 2Cit^{-3} + 4H_2O$	−17.81[a]
$Na_2C_2O_4 \rightleftharpoons 2Na^+ + C_2O_4^{2-}$	−1.68[a]

Values taken from: [a] Prywer *et al.* (2015).[61] [b] LNLL database. [c] Brečević *et al.* (1986).[62]

layer (diffusion boundary layer, DBL) at the reaction interface with a different composition to the bulk. First, calculations were done assuming values of the DBL thickness between 1 to 10 μm, which are typical for calcite dissolution under slightly acidic conditions[58–60] and considering the layer-by-layer dissolution of the calcite cleavage surface (*i.e.* the dissolution of calcite layers of 3.03 Å thickness) in the confined space of the DBL. These calculations allow an estimation of how many calcite layers should dissolve in order to reach saturation with respect to calcite in the DBL at the different pH values of the solutions used in the experiments, and the corresponding saturation index with respect to whewellite in the different conditions.

The latter can be estimated as: $SI = \log((a\mathrm{Ca}^{2+}{\cdot}a\mathrm{C_2O_4}^{2-})/K_{sp})$, where $a\mathrm{Ca}^{2+}$ and $a\mathrm{C_2O_4}^{2-}$ are the activities of calcium and oxalate ions and K_{sp} is the solubility product of whewellite at the given experimental conditions. Additionally, similar calculations were performed by fixing the concentration of oxalic acid at 25 mM and the pH at 2.5, and varying the citrate concentration from 0.001 to 100 mM. Citrate speciation as a function of pH was also modeled using *PHREEQc*.

Molecular dynamic modelling

Molecular simulations were performed in order to estimate the energy of the interaction between different citrate species and different whewellite faces. Whewellite was modelled according to the unit cell derived from the crystallographic data by Echigo *et al.* (2005).[63] From this unit cell, cleavage surfaces were built and the interaction energy ($E_{Interaction}$) calculated according to eqn (1):

$$E_{Interaction} = E_{Total} - (E_{Surface} + E_{Citrate}) \quad (1)$$

To obtain the energies from eqn (1), the modelled cleavage surfaces and the different citrate species were first geometrically optimized separately, put together in a continuous box and geometrically optimized again to obtain the position of the citrate species with respect to the whewellite surface. The energies for the global system (E_{Total}) and for each element separately ($E_{Surface}$ and $E_{Citrate}$) were calculated after dynamic simulations. All the simulations were performed with the Forcite Plus tools and the software Material Studio v8.0 (BIOVIA, San Diego, CA) under both the Universal Force Field (UFF)[64] and the *ab initio* Force Field COMPASS (Condensed-phase Optimized Molecular Potentials for Atomistic Simulation Studies). At least 4 layers of the whewellite unit cell were used to build the cleavage surfaces with and without relaxing the surface.

Results

When water was passed over the calcite surface in flow-through experiments, typical rhombohedral etch pits were observed nucleating and spreading on the surface as it dissolved (Fig. 1a). When test solutions containing 25 mM of oxalic acid (with and without citrate) were injected in the fluid cell, the immediate precipitation of a new phase (Fig. 1a) was always observed. From the comparison between the observed morphologies of the newly precipitated crystals and the whewellite equilibrium morphology simulated using SHAPE software (v7.4) (Fig. 1b) considering the $P2_1/c$ spatial group,[65] it seems that whewellite crystals precipitate in these experiments with the {100} surfaces parallel to the {10.4} calcite surface (Fig. 1c). Whewellite crystals have a homogeneous size and a perfect alignment over the calcite surface, with the $<001>_{whe}$ direction parallel to the $<010>_{cal}$ direction, as depicted in Fig. 1a.

The presence of whewellite together with calcite was confirmed by the powder X-ray diffraction analysis (Fig. 2) of randomly selected crystals after the AFM experiments.

The influence of pH on calcium oxalate precipitation

A first set of AFM flow through experiments were focused on studying the influence of pH on the precipitated calcium oxalate morphologies by varying the pH (in the range 1.75–4.50) of the inlet test solutions with a fixed oxalic acid concentration of 25 mM and three different citrate concentrations: 0, 0.1 and 10 mM.

In control runs (*i.e.* in the absence of citrate in the oxalate solution), it was observed the immediate precipitation of whewellite crystals with a slight increase in size with increasing pH. The crystal length (L), along the $<001>_{whe}$ direction increased from 360 to 420 nm, while the width (W), along the $<010>_{whe}$ direction, increased from 140 to 180 nm when the solution pH was changed from 1.75 up to 3.5 (Fig. 3a). For pH >

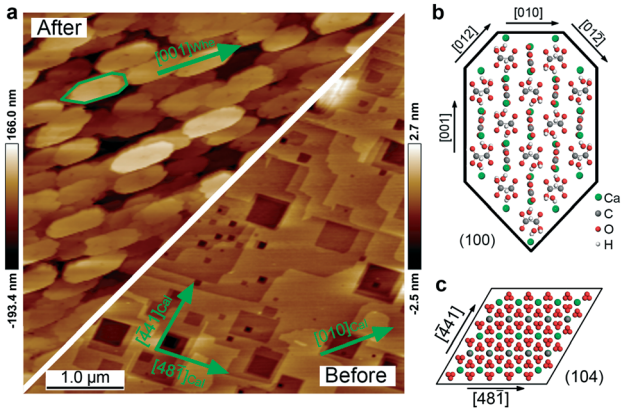

Fig. 1 a) AFM height image obtained before (bottom right corner) and after (upper left corner) test solutions entered the fluid cell of the AFM. The lower section shows typical calcite dissolution with the formation of rhombohedral etch pits. The upper section shows the coverage over the surface of whewellite crystals when an oxalate solution passed over the calcite surface. The darker the colour, the lower the height. b) Simulation of the whewellite habit and sketch of the structure of the (100) whewellite plane c) sketch showing the structure of the (104) calcite plane.

3.5 the crystal size increased noticeably (up to 1080 nm and 440 nm for the length and the width, respectively). However, a linear increase was found for the length to width ratio in the whole range of tested pH values. Additionally, at pH > 4, the previously coupled reaction involving the dissolution of calcite and the precipitation of whewellite was observed to be apparently uncoupled. Under these conditions, whewellite crystal precipitation started to occur far from the calcite {104} surface, presumably by spontaneous nucleation, and then settled on the calcite {10.4} surface. Whewellite crystals appeared on the surface as large (3.5 μm), randomly distributed crystals and lacking the observed preferential orientation of the whewellite crystals precipitated at pH < 4. As well, no orientation relationship was observed between the precipitated crystals and the calcite surface; moreover, the newly formed crystals were easily detached by the tip scanning movement, which suggests a weak binding on the calcite {10.4} surface. This, together with the increased crystal length (*ca.* 3.5 μm), made it almost impossible to scan an entire crystal at pH 4.5.

Interestingly, for a citrate concentration of 0.1 mM (Fig. 3b), a different trend in the length and width evolution with pH was found. The length of the precipitated whewellite crystals showed no significant changes with pH for pH < 2.5 and, from this value, it increased exponentially from 300 nm up to 3.15 μm at pH 4. Regarding the width, no significant changes with pH were found for pH < 3.5 and above this value it also started to increase exponentially from 180 nm up to 1.28 μm at pH 4.5, although at a slower rate than the increase in length. Likewise, observations showed that dissolution and precipitation were apparently uncoupled at pH > 4 in this set of experiments.

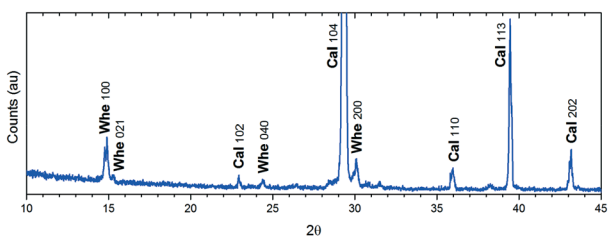

Fig. 2 Typical X-ray diffractogram of the calcite crystals after the AFM experiments. Whe (whewellite), Cal (calcite).

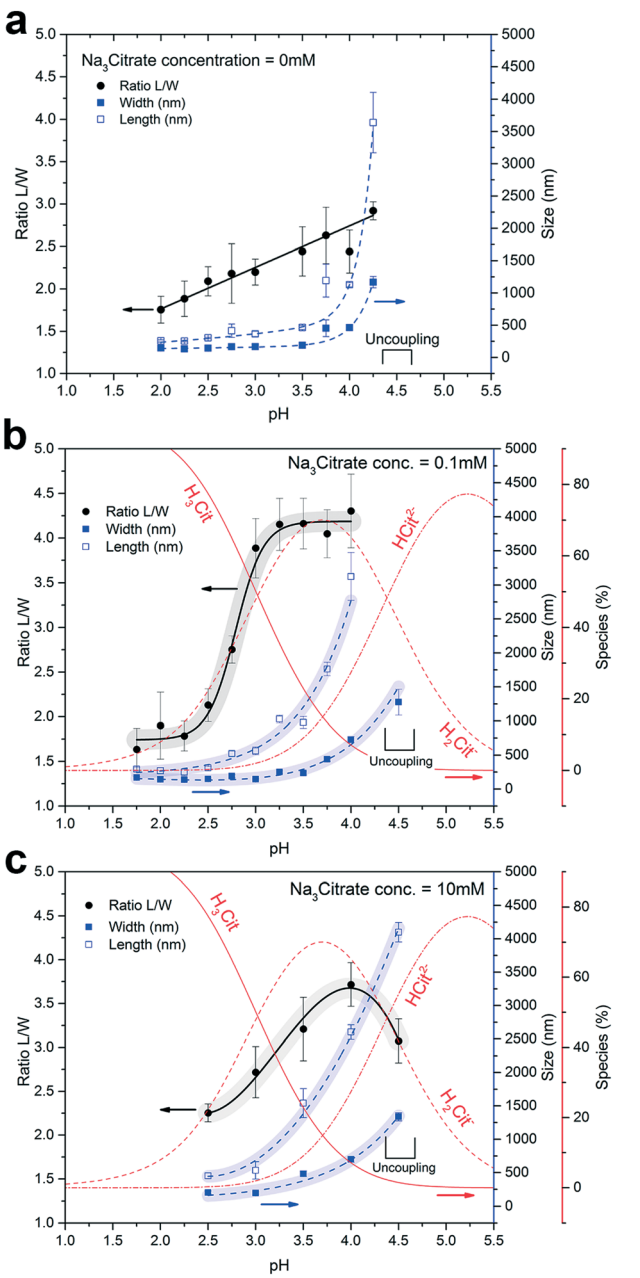

Fig. 3 Length (*L*), width (*W*) and the ratio between length and width (*L*/*W*) for precipitated whewellite crystals at different input solution pH values. Oxalic acid concentration = 25 mM. Citrate concentration: a) not present, b) 0.1 mM, c) 10 mM. Error bars show $2\sigma_N$. See ESI† for AFM images.

Finally, for the highest citrate concentration tested (10 mM), a similar trend to that observed at 0.1 mM in the crystal size (L and W) of the precipitates with pH was found, as seen in Fig. 3c. For this citrate concentration (10 mM) it was impossible to measure the L and W of the crystals precipitated on the calcite {10.4} surface at pH < 2.5 due to their undefined or amorphous-like morphologies. From pH 3, both L and W started to increase exponentially from 450 nm up to 4.20 μm and from 200 up to 1.35 μm (at pH 4.5), respectively.

Decoupling of dissolution and precipitation was observed again for pH > 4, but in this particular case it was possible to measure the size of some whewellite crystals before they were removed by the scanning of the AFM tip at pH 4.5.

Our speciation calculations using *PHREEQc*[57] (Fig. 4) confirm that a thin (1 to 10 μm thick) layer of fluid in contact with the mineral can become supersaturated with respect to whewellite under our experimental conditions before equilibrium with respect to calcite is reached, and also indicate that for pH < 3.5 the number of layers dissolved in this layer increase exponentially with decreasing pH.

Additionally, simplified molecular dynamics simulations were done to estimate the binding energy of different citrate species on different whewellite faces. As a result, it was found that for the H_2Cit^- species the strength of the binding energy with different whewellite faces follows the trend: {010} > {001} > {100} > {021} and for the $HCit^{2-}$ species: {001} > {021} > {100} > {010} as observed in Fig. 5. These two citrate species are the major species in the pH range of our experiments. Though not tested experimentally in our study, molecular simulations for the full deprotonated citrate species (Cit^{3-}) were also performed and the results were in agreement with those obtained by Qiu *et al.* (2005),[55] showing in both cases the same relative trends for the binding energies to the {010} and {100} faces.

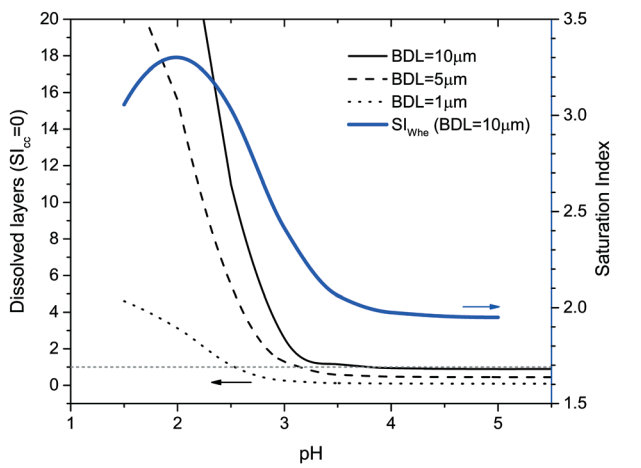

Fig. 4 Number of dissolved layers of calcite in order to reach saturation with respect to calcite in the DBL at different pH values in the range 1.5–5 and whewellite saturation index for different values of the DBL thickness (oxalic acid concentration = 25 mM, no citrate present).

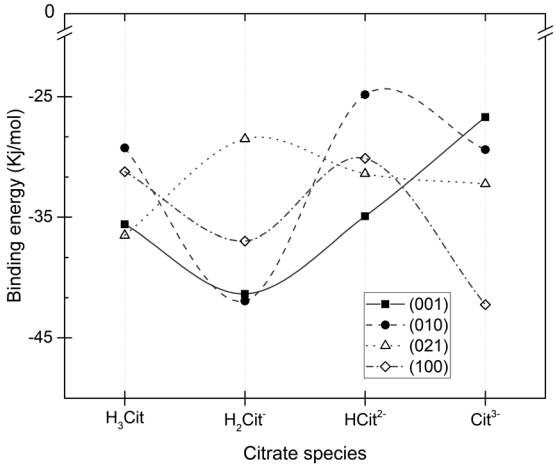

Fig. 5 Relative binding energies of different citrate species on the main whewellite faces derived from simplified molecular simulations.

Influence of citrate concentration on calcium oxalate precipitation

In order to investigate the effect of citrate concentration within the pH range where calcite dissolution and whewellite

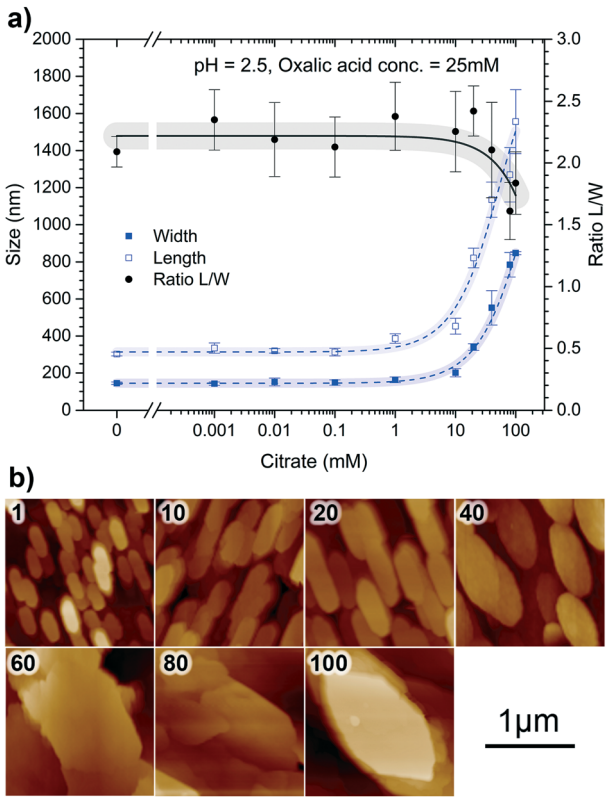

Fig. 6 Influence of citrate on precipitated whewellite crystal size (pH = 2.5, oxalic acid concentration = 25 mM). a) Measurements from the *in situ* AFM direct observations. Error bars show $2\sigma_N$. b) AFM height images of the whewellite crystals precipitated during flow-through experiments (upper-left side of every image shows citrate concentration in mM). See ESI† for more images.

precipitation are coupled, a set of experiments were performed varying the citrate concentration between 1 μM and 100 mM, while keeping the pH and oxalic acid concentration constant at 2.5 and 25 mM, respectively. As presented in Fig. 6, the measured sizes and length to width ratios of the precipitated whewellite crystals seem to be constant up to a citrate concentration of 1 mM. For citrate concentrations above 1 mM, the precipitated whewellite crystals increased in size and showed a linear decrease (note that in Fig. 4 the *x*-axis is logarithmic) in the length to width ratio with increasing citrate concentration, resulting in rounded morphologies but still showing some straight edges as observed in Fig. 6b. For citrate concentrations higher than 40 mM, the precipitated whewellite crystals did not appear to be oriented on the calcite {10.4} surface; additionally, they were found to easily become detached from the calcite surface due to the AFM tip movement during the scanning of the surface (Fig. 6). *PHREEQc* simulations performed allowing equilibration with respect to calcite in the confined space of a DBL of 10 μm, indicate (Fig. 7) that for citrate concentrations higher than 1 mM, the ionic strength and the dissolved amount of calcite increase dramatically while the saturation index for whewellite decreases, as has been also experimentally reported by Oelkers *et al.* (2011).[36]

Additionally, if we compare the evolution of citrate speciation with pH with the crystal size measurements from the AFM experiments, it can be observed (Fig. 3) how both the length of the whewellite crystals and H_2Cit^- species increase in parallel. With increasing pH, the $HCit^{2-}$ becomes the major species, and the width of the crystals also increases. It is also observed that the evolution in the length to width ratio (*L*/*W*) of the whewellite crystals with pH in the range 1.75–4.00, perfectly matches the evolution of the $H2Cit^-$ concentration with pH (Fig. 3b).

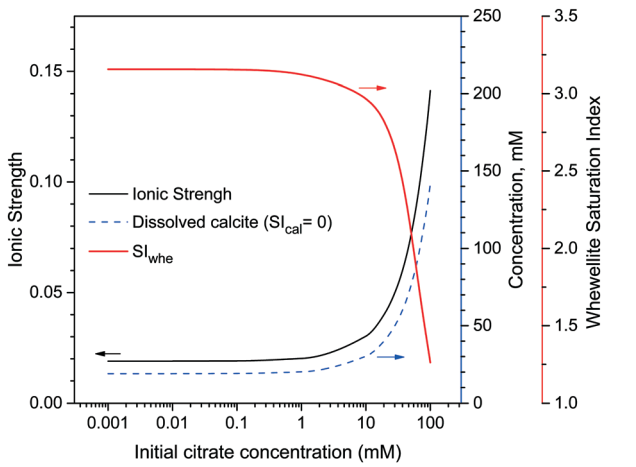

Fig. 7 Results of the calculations performed using the PHREEQc geochemical code (allowing equilibration with respect to calcite for a DBL of 10 μm): evolution of ionic strength (dimensionless), whewellite saturation index (mM) and dissolved amount of calcite (mM) as a function of initial citrate concentration (1 μM–100 mM). Calculations were performed for an initial oxalic acid concentration of 25 mM and a pH of 2.5.

Discussion

Mechanism of the replacement of calcite by whewellite

Our observations provide direct experimental evidence confirming that under the given solution conditions and at pH below 4, the precipitation of whewellite on calcite surfaces exposed to oxalate solutions occurs by an interface-coupled dissolution of the calcite surface and subsequent whewellite precipitation, as deduced from previous indirect experimental observations.[66,67] During this coupled process the bulk solution passing over the calcite surface was undersaturated with respect to whewellite. This implies that the solution at the mineral–solution interface must have become supersaturated with respect to the precipitating phase.[21] This could occur if dissolution of calcite (*i.e.* the release of Ca^{2+} ions) is faster than diffusion of released ions away from the dissolving calcite surface. The dissolution of a few monolayers of dissolved calcite can be sufficient to release enough Ca^{2+} ions to the mineral–solution interface in order to enable supersaturation to be reached with respect to different calcium oxalate phases in a thin layer of solution in contact with the mineral surface.[21]

This is also confirmed by the results of the *PHREEQc*[57] calculations performed (see above). The nucleation rate of whewellite (the product phase) will thus be controlled by the supersaturation of the calcite–solution boundary layer with respect to this phase.[68] The epitaxial growth of whewellite on a calcite surface is further promoted, but not limited, by the structural matching existing between calcite and whewellite,[66] which results in a reduction in the interfacial energy at this new interface.[69] Note that, although the epitaxial growth of whewellite on calcite has not been studied for planes different to the calcite cleavage plane, it has been reported that, in more complex polycrystalline systems, such as marble, the use of low pH oxalate solutions resulted in the pseudomorphic replacement of the substrate by continuous and regular calcium oxalate rims that developed on the marble surface regardless of the exposed calcite plane.[24,67]

Therefore, the fluid composition at the interface will be a key factor controlling the coupling between calcite dissolution and whewellite precipitation reaction. A replacement reaction occurs by an interface-coupled dissolution–precipitation mechanism whenever the rate of dissolution and precipitation are coupled at the reaction interface.[19,21] On the other hand, changes in pH have been previously suggested to affect the coupling between dissolution and precipitation at the mineral–fluid interface during replacement reactions.[66,70] As suggested by our previous work,[66] the observations reported here confirm that pH plays a key role in the coupling between dissolution and precipitation reactions during the replacement of calcite by whewellite.

Formation of compositional gradients during mineral replacement reactions

Dissolution of a solid surface in contact with a fluid is a two-step process: the release of ions from the solid and the

subsequent diffusion of these ions into the bulk solution. If no other ions (different to those building the solid) were present, the dissolution of the parent surface would slow down and eventually stop when the solution in contact with the mineral approaches saturation and then becomes saturated with respect to the dissolving mineral. In our system, however, ions present in the solution surrounding the mineral substrate (oxalate and citrate) interact with the Ca^{2+} ions released from the calcite surface resulting in supersaturation with respect to a new Ca-oxalate phase, which can then precipitate. Precipitation of a Ca-oxalate phase (less soluble than the original calcite), reduces the ionic concentration at the interface, which allows further dissolution of calcite. This in turn results in an interface-coupled dissolution–precipitation process, ultimately controlled by the solution composition of the DBL.

Our speciation calculations show that (i) supersaturation with respect to whewellite can be reached in the DBL, and (ii) the amount of Ca^{2+} ions available in the DBL is higher at low pH values, indicating that higher supersaturation values with respect to whewellite are reached at low pH values. The higher the supersaturation with respect to whewellite in the DBL, the greater the possibility that whewellite spontaneously nucleates and precipitates. As well, the higher the supersaturation with respect to whewellite, the higher the nucleation density of whewellite, but the smaller the size of the crystals[68] because of kinetic considerations. Once the calcite surface is fully covered by whewellite crystals, it could become passivated from further dissolution and so the interface-coupled dissolution–precipitation process could eventually slow down or even cease.

Moreover, in the absence of any additive (citrate in our case), the relative rates of calcite dissolution and ion diffusion towards the bulk solution will determine the local supersaturation with respect to whewellite in the fluid in contact with the mineral and thus the rate of whewellite precipitation. In order to preserve the texture of the parent mineral, dissolution and precipitation reactions must be spatially coupled, *i.e.* they must occur close to each other. This requires fast nucleation of whewellite near the dissolving calcite surface,[71] which occurs when dissolution releasing ions is the rate-limiting step, so that high supersaturation values with respect to whewellite are achieved locally and temporally in the vicinity of the dissolving mineral surface. This occurs in our system under low pH (4 or lower) conditions, when calcite dissolves faster. Whewellite will thus nucleate spontaneously and precipitate, preserving the crystallographic information of the parent mineral, as observed in AFM experiments. This coupling between calcite dissolution and whewellite precipitation allows the formation of pseudomorphs.

Finally, for pH $\geq$ 4.5 calcite dissolves more slowly and uncoupling of dissolution and precipitation reactions was observed during AFM flow-through experiments. At these higher pH values, the diffusion of the ions towards the bulk solution became almost as fast as the detachment of new ions from the dissolving surface, and the process becomes controlled by the rate of whewellite precipitation. Whewellite started to precipitate at a slower rate and far from the surface, showing bigger crystal sizes (larger than 3.5 μm). At pH $>$ 4.5, this results in the loss of the preferential orientation of the whewellite crystals on the calcite surface seen at lower pH values. These new whewellite crystals now appear randomly distributed on the calcite surface, leading to poor preservation of the fine textures of the original mineral substrate.

The influence of citrate on the replacement of calcite by whewellite

Citrate is known to exert an inhibitory effect on calcium oxalate crystallization.[38] Qiu *et al.* (2005)[55] found that citrate controls the habit and kinetics of whewellite growth mostly by step pinning on different faces through specific surface interactions. Additionally, on renal tubular cells citrate may disrupt the adhesive forces existing between whewellite crystals and cells by calcium chelation and/or charge neutralization which results in crystal detachment.[51] However, it should be considered that in our system, the low citrate concentrations show only morphological effects in the precipitated whewellite crystals. Our AFM observations indicate that the addition of citrate and the changes in its speciation as a function of pH have a marked influence on the replacement process of calcite by whewellite (Fig. 3).

Indeed, our results suggest that the different citrate species are preferentially adsorbed onto different whewellite crystallographic faces, as explained below. From the molecular-scale point of view, the interaction between whewellite surfaces and citrate will take place through the electrostatic interaction between COO– groups from citrate molecules and Ca^{2+} ions on the whewellite crystal surface, and/or the establishment of H-bonds between the OH^- groups of citrate and water molecules in the oxalate ions.[55] The latter is in agreement with results from molecular dynamic simulations (Fig. 5). At pH $<$2.5, H_3Cit is the major citrate specie which, according to estimated binding energies,

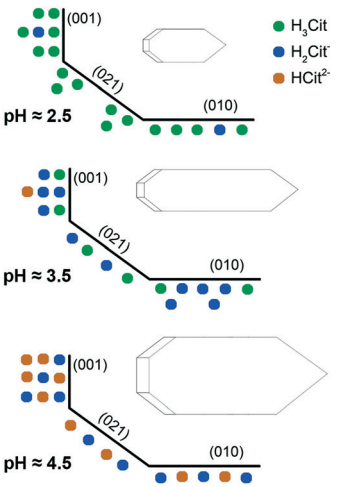

Fig. 8 Schematic representation of the modification of whewellite crystal morphology due to the preferential face-specific adsorption of different citrate species. Color dots represent the relative affinity of different citrate species to adsorb onto different whewellite faces.

would preferentially adsorb onto {001} and {021} whewellite faces. On the other hand, H_2Cit^- (which is the dominant specie in the 2.8 to 4.3 pH range) adsorption is more energetically favorable onto {010} and {001} whewellite faces. With increasing pH, the H_3Cit concentration starts to decrease while H_2Cit^- starts to increase, thus decreasing the overall citrate adsorption on {021} and increasing citrate adsorption on {010} (Fig. 8). This may explain the elongation of the whewellite crystals and the increasing *L*/*W* ratios with increasing pH. On the other hand, increasing the citrate concentration leads to lower $SI_{whewellite}$ and therefore, to larger crystal sizes. As well, increasing citrate concentration would imply increasing citrate adsorption and thus, as seen in Fig. 6, would result at pH = 2.5 (when H_3Cit is the dominant specie) in crystals with lower *L*/*W* ratios, in agreement with our experimental results obtained in the presence of [citrate] = 10 mM (Fig. 3c), when lower *L*/*W* ratios were systematically found compared to experiments performed with [citrate] = 0.1 mM (Fig. 3b). However, at both citrate concentrations, similar trends in the *L*/*W* ratio in the 2.5 to 4.0 pH range were obtained. Additionally, for pH = 4.5 and at [citrate] = 10 mM, *L*/*W* ratios were observed to decrease again. The latter is in agreement with the reduction in the H_2Cit^- concentration and the increasing $HCit^{2-}$ concentration, which is again preferentially adsorbed onto {001} and {021} whewellite faces (Fig. 5), resulting in a decrease in the growth rate along the $<001>_{whe}$ directions.

As shown by our PHREEQc simulations, for a fixed pH, the presence of citrate in concentrations higher than 1 mM increases the amount of calcite dissolved before equilibrium with respect to calcite is achieved. This in principle should lead to higher supersaturation values with respect to whewellite. However, the complexing of the citrate with Ca^{2+} reduces the free calcium in solution and leads to an effective reduction in the supersaturation with respect to whewellite (Fig. 7). The latter results in a slower nucleation and growth rate and hence in larger crystal sizes and lower nucleation density in the presence of citrate, as directly observed in our AFM experiments (Fig. 6b). Moreover, for citrate concentrations above 40 mM uncoupling between dissolution and precipitation is observed even under these low pH conditions when the preferential orientation of whewellite crystals onto calcite is no longer observed (Fig. 6b), as revealed by the departure from the parallel alignment of the $<001>_{whe}$ direction of the precipitated whewellite crystals and the $<010>_{cal}$ direction of the calcite substrate. These effects are thus direct consequence of the slower precipitation rate of whewellite due to the lower supersaturation values with respect to whewellite achieved in the fluid directly in contact with the calcite surface when citrate is present. Citrate effectively acts as an inhibitor for the growth of whewellite.

Conclusions

The present work provides direct experimental evidence confirming the key role of the aqueous solution composition during mineral replacement reactions, in particular in the coupling between dissolution and precipitation reactions. The dissolution of calcite releases Ca^{2+} ions that then combine with oxalate ions in solution resulting in precipitation of whewellite on the dissolving calcite surfaces. At low pH values, the dissolution of calcite is faster than the diffusion of these ions to the bulk solution, allowing the build-up, close to the mineral surface, of high calcium concentrations and supersaturation values with respect to whewellite. This ultimately results in the fast precipitation of whewellite, spatially coupled to calcite dissolution, right at the interface between the mineral surface and the fluid. For pH values higher than 4, the calcite dissolution rate starts to decrease and whewellite precipitation takes place at a slower rate away from the dissolving surface, resulting in the uncoupling between dissolution and precipitation processes as directly observed in AFM experiments.

The pH of the solution plays an important role in the specific interaction between citrate and the newly formed whewellite crystals, and the subsequent effect of citrate on their size and morphology, due to the effect of pH on citrate speciation (Fig. 8).

The presence of citrate enhances calcite dissolution (Fig. 7), but citrate tends also to complex the Ca^{2+} released upon calcite dissolution,[48,55] overall resulting in a reduction in $SI_{whewellite}$ and in larger whewellite crystal sizes.

Regarding the implications of our findings for the conservation of cultural heritage, our results suggest that the combination of low pH values and the addition of an organic molecule such as citrate at a concentration below 10 mM could be suitable to achieve a coherent protective layer that preserves the textures of the original surface. This is obtained by the control of the orientation, size and morphology of whewellite crystals precipitated as a result of the interaction of an oxalate solution and calcareous surfaces. The production of a Ca-oxalate layer on calcareous building stones (marble and limestones commonly used as building material) can therefore be designed and controlled by a careful selection of the solution composition. Ideally, a continuous and coherent surface layer of a Ca-oxalate phase formed by an interface-coupled dissolution–precipitation process would protect the underlying stone from further attack from environmental solutions.[24] With this knowledge, new functional materials could be successfully designed and used in the preservation of the cultural heritage.

Acknowledgements

This research was done within the grants MAT2012-37584 and P11-RNM-7550, funded by the Spanish Government, European Commission (ERDF funds) and the Junta de Andalucía. Additional funding was provided by the research group RNM-179 of the Junta de Andalucía and the Unidad Científica de Excelencia UCE-PP2016-05 of the University of Granada for financial support. ER-A acknowledges the receipt of a *Ramón y Cajal* grant from the Spanish Government (*Ministerio de Economía y*

Competitividad) and CVP acknowledges funding from the EU initial training networks *CO2React* and *Flowtrans*.

References

1 C. Y. Pak, *Lancet*, 1998, **351**, 1797–1801.
2 M. Masár, M. Žúborová, D. Kaniansky and B. Stanislawski, *J. Sep. Sci.*, 2003, **26**, 647–652.
3 V. R. Franceschi and P. A. Nakata, *Annu. Rev. Plant Biol.*, 2005, **56**, 41–71.
4 B. Serdar and H. Demiray, *Turk. J. Biol.*, 2012, **36**, 386–393.
5 N.-O. Nilvebrant, A. Reimann, F. de Sousa, S. Larsson, P. Cassland, F. Hong and L. J. Jönsson, in *Biotechnology in the Pulp and Paper Industry*, ed. L. Viikari and R. Lantto, Elsevier Science B.V., 2002, pp. 231–238.
6 A. Sjöde, S. Winestrand, N. O. Nilvebrant and L. J. Jönsson, *Enzyme Microb. Technol.*, 2008, **43**, 78–83.
7 C. O. Perera, I. C. Hallett, T. T. Nguyen and J. C. Charles, *J. Food Sci.*, 1990, **55**, 1066–1069.
8 K. D. Demadis and M. Öner, in *Green Chemistry Research Trends*, ed. J. T. Pearlman, Nova Science Publishers, Inc., 2009, pp. 265–287.
9 D. S. Milliner, *Calcium Oxalate Biol. Syst.*, 1995, 169–188.
10 J. P. Kavanagh, L. Jones and P. N. Rao, *Clin. Sci.*, 2000, **98**, 151–158.
11 P. Maravelaki-Kalaitzaki, *Anal. Chim. Acta*, 2005, **532**, 187–198.
12 J. Loret, J. T. Tanacredi and T. Heritage, *Nature*, 1892, **46**, 258–260.
13 M. Del Monte, C. Sabbioni, G. Zappia, M. D. E. L. Monte, U. Bologna, C. Sabbioni, G. Zappia, U. Bologna, M. Del Monte, C. Sabbioni, G. Zappia, M. D. E. L. Monte and U. Bologna, *Sci. Total Environ.*, 1987, **67**, 17–39.
14 M. Del Monte and C. Sabbioni, *Environ. Sci. Technol.*, 1983, **17**, 518–522.
15 T. Rosado, M. Gil, J. Mirão, A. Candeias and A. T. Caldeira, *Int. Biodeterior. Biodegrad.*, 2013, **85**, 1–7.
16 M. Monte, *J. Cult. Herit.*, 2003, **4**, 255–258.
17 C. Sabbioni and G. Zappia, *Aerobiologia*, 1991, **7**, 31–37.
18 G. M. Gadd, J. Bahri-Esfahani, Q. Li, Y. J. Rhee, Z. Wei, M. Fomina and X. Liang, *Fungal Biol. Rev.*, 2014, **28**, 36–55.
19 A. Putnis, *Rev. Mineral. Geochem.*, 2009, **70**, 87–124.
20 C. V. Putnis and E. Ruiz-Agudo, *Elements*, 2013, **9**, 177–182.
21 E. Ruiz-Agudo, C. V. Putnis and A. Putnis, *Chem. Geol.*, 2014, **383**, 132–146.
22 C. Conti, C. Colombo, D. Dellasega, M. Matteini, M. Realini and G. Zerbi, *J. Cult. Herit.*, 2011, **12**, 372–379.
23 C. Conti, I. Aliatis, M. Casati, C. Colombo, M. Matteini, R. Negrotti, M. Realini and G. Zerbi, *J. Cult. Herit.*, 2014, **15**, 336–338.
24 A. Burgos-Cara, E. Ruiz-Agudo and C. Rodriguez-Navarro, *Mater. Des.*, 2017, **115**, 82–92.
25 A. Putnis, *Mineral. Mag.*, 2002, **66**, 689–708.
26 K. Pollok, C. V. Putnis and A. Putnis, *Am. J. Sci.*, 2011, **311**, 211–236.
27 G. Graziani, E. Sassoni, E. Franzoni and G. W. Scherer, *Appl. Surf. Sci.*, 2016, **368**, 241–257.
28 K. Chatzipanagis, M. Iafisco, T. Roncal-Herrero, M. Bilton, A. Tampieri, R. Kröger and J. M. Delgado-López, *CrystEngComm*, 2016, **18**, 3170–3173.
29 J. Klasa, E. Ruiz-Agudo, L. J. J. Wang, C. V. V. Putnis, E. Valsami-Jones, M. Menneken and A. Putnis, *Geochim. Cosmochim. Acta*, 2013, **117**, 115–128.
30 L. Wang, S. Li, E. Ruiz-Agudo, C. V. Putnis and A. Putnis, *CrystEngComm*, 2012, **14**, 6252.
31 L. Wang, E. Ruiz-Agudo, C. V. Putnis, M. Menneken and A. Putnis, *Environ. Sci. Technol.*, 2012, **46**, 834–842.
32 K. R. Cho, E. A. Salter, J. J. De Yoreo, A. Wierzbicki, S. Elhadj, Y. Huang and S. R. Qiu, *CrystEngComm*, 2012, **15**, 54–64.
33 E. Akyol and M. Öner, *J. Cryst. Growth*, 2007, **307**, 137–144.
34 D. J. Tobler, J. D. R. Blanco, K. Dideriksen, K. K. Sand, N. Bovet, L. G. Benning and S. L. S. Stipp, *Procedia Earth Planet. Sci.*, 2014, **10**, 143–148.
35 C. Rodriguez-Navarro, A. Burgos Cara, K. Elert, C. V. Putnis and E. Ruiz-Agudo, *Cryst. Growth Des.*, 2016, **16**, 1850–1860.
36 E. H. Oelkers, S. V. Golubev, O. S. Pokrovsky and P. Bénézeth, *Geochim. Cosmochim. Acta*, 2011, **75**, 1799–1813.
37 E. Konya, T. Umekawa, M. Iguchi and T. Kurita, *Eur. Urol.*, 2003, **43**, 564–571.
38 L. Wang, W. Zhang, S. R. Qiu, W. J. Zachowicz, X. Guan, R. Tang, J. R. Hoyer, J. J. De Yoreo and G. H. Nancollas, *J. Cryst. Growth*, 2006, **291**, 160–165.
39 A. Neira-Carrillo, F. Luengo-Ponce, P. Vásquez-Quitral, M. Yazdani-Pedram, M. S. Fernández, H. Cölfen and J. L. Arias, *Eur. J. Inorg. Chem.*, 2015, **2015**, 1167–1177.
40 B. Hess, L. Zipperle and P. Jaeger, *Am. J. Physiol.*, 1993, **265**, F784–791.
41 F. Atmani, B. Lacour, P. Jungers, T. Drüeke and M. Daudon, *Urol. Res.*, 1994, **22**, 257–260.
42 S. Ebisuno, K. Miyata, Y. Kohjimoto and T. Ohkawa, *Nippon Hinyokika Gakkai Zasshi*, 1993, **84**, 339–344.
43 H. Shiraga, W. Min, W. J. VanDusen, M. D. Clayman, D. Miner, C. H. Terrell, J. R. Sherbotie, J. W. Foreman, C. Przysiecki and E. G. Neilson, *Proc. Natl. Acad. Sci. U. S. A.*, 1992, **89**, 426–430.
44 L.-C. Su, Z. Xie, Y. Zhang, K. T. Nguyen and J. Yang, *Front. Bioeng. Biotechnol.*, 2014, **2**, 23.
45 A. Allende, J. McEvoy, Y. Tao and Y. Luo, *Food Control*, 2009, **20**, 230–234.
46 M. Hajir, R. Graf and W. Tremel, *Chem. Commun.*, 2014, **50**, 6534–65366.
47 D. J. Tobler, J. D. Rodriguez-Blanco, K. Dideriksen, N. Bovet, K. K. Sand and S. L. S. Stipp, *Adv. Funct. Mater.*, 2015, **25**, 3081–3090.
48 J. M. Delgado-López, R. Frison, A. Cervellino, J. Gómez-Morales, A. Guagliardi and N. Masciocchi, *Adv. Funct. Mater.*, 2014, **24**, 1090–1099.
49 J. M. Delgado-López, M. Iafisco, I. Rodríguez, A. Tampieri, M. Prat and J. Gómez-Morales, *Acta Biomater.*, 2012, **8**, 3491–3499.
50 M. Iafisco, G. B. Ramírez-Rodríguez, Y. Sakhno, A. Tampieri, G. Martra, J. Gómez-Morales and J. M. Delgado-López, *CrystEngComm*, 2015, **17**, 507–511.

51 S. Chutipongtanate, S. Chaiyarit and V. Thongboonkerd, *Eur. J. Pharmacol.*, 2012, **689**, 219–225.

52 R. L. Ryall, R. M. Harnett and V. R. Marshall, *Clin. Chim. Acta*, 1981, **112**, 349–356.

53 E. Ruiz-Agudo and C. V. Putnis, *Mineral. Mag.*, 2012, **76**, 227–253.

54 S. Guo, M. D. Ward and J. A. Wesson, *Langmuir*, 2002, **18**, 4284–4291.

55 S. R. Qiu, A. Wierzbicki, E. A. Salter, S. Zepeda, C. A. Orme, J. R. Hoyer, G. H. Nancollas, A. M. Cody and J. J. De Yoreo, *J. Am. Chem. Soc.*, 2005, **127**, 9036–9044.

56 M. L. Weaver, S. R. Qiu, J. R. Hoyer, W. H. Casey, G. H. Nancollas and J. J. De Yoreo, *J. Cryst. Growth*, 2007, **306**, 135–145.

57 D. L. Parkhurst and C. A. J. Appelo, *Description of input and examples for PHREEQC version 3--A computer program for speciation, batch-reaction, one-dimensional transport, and inverse geochemical calculations*, 2013.

58 Z. Liu and W. Dreybrod, *Geochim. Cosmochim. Acta*, 1997, **61**, 2879–2889.

59 S. Sizaret, I. Fedioun, L. Barbanson and Y. Chen, *Geophys. J. Int.*, 2006, **167**, 1027–1034.

60 M. D. Covington, *Acta Carsologica*, 2014, **43**, 195–202.

61 J. Prywer, M. Olszynski and E. Mielniczek-Brzóska, *J. Solid State Chem.*, 2015, **231**, 80–86.

62 L. Brečević, D. Škrtić and J. Garside, *J. Cryst. Growth*, 1986, **74**, 399–408.

63 T. Echigo, M. Kimata, A. Kyono, M. Shimizu and T. Hatta, *Mineral. Mag.*, 2005, **69**, 77–88.

64 A. K. Rappe, C. J. Casewit, K. S. Colwell, W. A. Goddard and W. M. Skiff, *J. Am. Chem. Soc.*, 1992, **114**, 10024–10035.

65 A. Millan, *Cryst. Growth Des.*, 2001, **1**, 245–254.

66 E. Ruiz-Agudo, P. Álvarez-Lloret, C. V. Putnis, A. B. Rodriguez-Navarro and A. Putnis, *CrystEngComm*, 2013, **15**, 9968.

67 H. E. King, D. C. Mattner, O. Plümper, T. Geisler and A. Putnis, *Cryst. Growth Des.*, 2014, **14**, 3910–3917.

68 R. Lacmann, A. Herden and C. C. Mayer, *Chem. Eng. Technol.*, 1999, **22**, 279–289.

69 A. Putnis, *Introduction to mineral sciences*, Cambridge University Press, Cambridge, 1992.

70 F. Xia, J. Brugger, G. Chen, Y. Ngothai, B. O'Neill, A. Putnis and A. Pring, *Geochim. Cosmochim. Acta*, 2009, **73**, 1945–1969.

71 A. Altree-Williams, A. Pring, Y. Ngothai and J. Brugger, *Earth-Sci. Rev.*, 2015, **150**, 628–651.